Numerical Analysis of a Cartridge in the Traveling Liquidus-Zone Method under Various Gravity Conditions

Satoshi Adachi [1], Shin-ichi Yoda [2], and Kyoichi Kinoshita [2]

[1] Space Utilization Research Center, Office of Space Utilization Systems, National Space Development Agency of Japan, 2-1-1, Sengen, Tsukuba-shi, Ibaraki, 305-8505 Japan

[2] Space Utilization Research Program, National Space Development Agency of Japan, 2-1-1, Sengen, Tsukuba-shi, Ibaraki, 305-8505 Japan

Abstract

To obtain temperature and concentration distributions and to understand convective flow pattern in the case of traveling liquidus-zone (TLZ) method, numerical analyses under various gravity conditions have been carried out. The calculation code is developed based on the boundary fitted coordinate (BFC) method. Quasi-equilibrium state at the interfaces is assumed in order to determine temperature and concentration at the interfaces. By using the developed code, time evolution of temperature, concentration, a stream function, vorticity, and an interface location are obtained. From calculation results, several features are found; (i) the width initially decreases and then begins to increase at a certain time under the higher gravity condition, although the zone width continuously decreases under the lower gravity condition, (ii) supercooling region around axis in the zone can be reduced under the low gravity condition.

Introduction

The traveling liquidus-zone (TLZ) method [1)] is one of the most promising growth techniques to obtain a homogeneous single crystal of a ternary compound semiconductor. By applying the TLZ method to crystal growth of an InGaAs compound semiconductor on the earth, single crystals of 2 mm in diameter and uniform composition of around 0.3 of indium are obtained. The most valuable feature of the TLZ method is that the solution concentration is saturated and sustained at the concentration determined by the liquidus in the whole zone region. Namely, the concentration distribution can be controlled by the temperature distribution only. This means that if a linear temperature profile is used and if the temperature difference between a seed and a feed is small, a concentration profile also becomes nearly linear, because the liquidus can be approximately linear within a narrow temperature range. Since many conventional growth techniques control temperature and concentration distributions separately, crystal growth with uniform compositions is much difficult in the conventional cases as compared with the TLZ method.

Although the TLZ method has several advantages to growth of homogeneous single crystals, applicable limitations, which is predicted by one-dimensional theory, such as maximum zone width or maximum growth length should be investigated. Although the TLZ may fail when the concentration distribution is not linear for the linear temperature gradient, in order to discuss the

limitation quantitatively, the theory should be verified by comparing with experimental data.

In order to verify the theory, microgravity experiments have been planned. Under the microgravity condition, heat and mass transports will be axisymmetric. Therefore if the condition of negligibly small radial dependencies is achieved, one-dimensional theory, which has been already provided, is easily and precisely compared with the experimental data. The radial dependencies mean a radial temperature gradient, a radial concentration gradient, and a curvature of a solid-liquid interface shape.

In order to perform the microgravity experiments, an ampoule and a cartridge, which are optimized for the flight experiments, must be designed. In order to design the ampoule and the cartridge, numerical calculation codes have been developed and improved. The code has been improved so as to calculate the TLZ growth and to solve the simultaneous governing equations of the energy transport, the mass transport, the vorticity transport, and the stream function.

To optimize the ampoule and the cartridge, understanding of the TLZ behavior under various gravity conditions should be deepened first. The behavior includes flow patterns, interface shapes, concentration distributions, temperature distributions, zone width, growth rates, and degree of supercooling. In this study, such the TLZ behavior under various gravity conditions is numerically investigated in the case of a candidate for a flight cartridge.

In this paper, the mathematical model is described in the next section, and then the calculation results under the various gravity conditions are described. After that, discussion and conclusions are described.

Mathematical Model

The numerical code must treat the TLZ method. The configuration of the TLZ method is the same as the temperature gradient zone method, which is one of the solution growth techniques. Namely, a solution zone is arranged between a seed and a feed. This means that there are two interfaces, that is, a seed-liquid interface and a feed-liquid one.

The governing equations are the energy transport equation, the mass transport equation, the vorticity transport equation, the stream function equation, the energy balance equation and the mass balance equation. These equations are represented as follows;

$$\begin{aligned}&\rho\, C_p \frac{\partial T}{\partial t} \\ &+\rho\, C_p\left(\frac{1}{r}\frac{\partial \psi}{\partial z}\frac{\partial T}{\partial r}-\frac{1}{r}\frac{\partial \psi}{\partial r}\frac{\partial T}{\partial z}\right), \\ &=\kappa\left(\frac{\partial^2 T}{\partial r^2}+\frac{1}{r}\frac{\partial T}{\partial r}+\frac{\partial^2 T}{\partial z^2}\right)\end{aligned} \tag{1}$$

$$\begin{aligned}&\frac{\partial T}{\partial t}+\left(\frac{1}{r}\frac{\partial \psi}{\partial z}\frac{\partial C_i}{\partial r}-\frac{1}{r}\frac{\partial \psi}{\partial r}\frac{\partial C_i}{\partial z}\right) \\ &=D_i\left(\frac{\partial^2 C_i}{\partial r^2}+\frac{1}{r}\frac{\partial C_i}{\partial r}+\frac{\partial^2 C_i}{\partial z^2}\right), \\ &(i=S \text{ or } L),\end{aligned} \tag{2}$$

$$\begin{aligned}&\frac{\partial \omega}{\partial t}+\frac{1}{r}\frac{\partial \psi}{\partial z}\frac{\partial \omega}{\partial r}-\frac{1}{r}\frac{\partial \psi}{\partial r}\frac{\partial \omega}{\partial z} \\ &-\frac{1}{r^2}\omega\frac{\partial \psi}{\partial z} \\ &=\nu\left(\frac{\partial^2 \omega}{\partial r^2}+\frac{1}{r}\frac{\partial \omega}{\partial r}+\frac{\partial^2 \omega}{\partial z^2}-\frac{1}{r^2}\omega\right), \\ &+B\,g\frac{\partial T}{\partial r}+G\,g\frac{\partial C_L}{\partial r}\end{aligned} \tag{3}$$

$$-r\omega=\frac{\partial^2 \psi}{\partial r^2}-\frac{1}{r}\frac{\partial \psi}{\partial r}+\frac{\partial^2 \psi}{\partial z^2}, \tag{4}$$

$$L_{SL}\,\rho\,\boldsymbol{u}\cdot\hat{\boldsymbol{n}} = -\kappa_L\left(\frac{\partial T}{\partial n}\right)_L + \kappa_S\left(\frac{\partial T}{\partial n}\right)_S, \text{ and} \qquad (5)$$

$$\left(C_L - C_S\right)\boldsymbol{u}\cdot\hat{\boldsymbol{n}} = -D_L\left(\frac{\partial C_L}{\partial n}\right)_L, \qquad (6)$$

where, ψ is the stream function, ω vorticity, T temperature, ρ density, C_p specific heat, κ thermal conductivity, ν kinetic viscosity, L_{SL} latent heat, B thermal volume expansion coefficient, G the buoyancy coefficient by the specific gravity difference, g gravity, r radius, z length, t time, C the concentration, $\boldsymbol{u}$ moving velocity vector of the interface, $\hat{\boldsymbol{n}}$ normal unit vector to the interface, D the diffusion coefficient. Subscripts of L and S indicate the liquid side and the solid side, respectively. In this study, the governing equations are expressed by using the cylindrical coordinates so as to match a typical flight sample shape.

In order to obtain temperatures and concentrations in the liquid and the solid at the interface, Eqs. (5) and (6) are solved simultaneously. In Eqs. (5) and (6), however, there are three variables. Therefore additional relationship is required. In this study, a phase diagram is used as the additional relationship. By using the phase diagram of InGaAs [2] as shown in Fig. 1, the relationships between the concentration in the solid and the temperature, and between the concentration in the liquid and the temperature can be described as

$$C_S = f_S(T), \text{ and} \qquad (7)$$

$$C_L = f_L(T), \qquad (8)$$

where f_S and f_L represent the solidus and the liquidus. Figure 1 is an inverse plot as compared with a usual plot, that is, the horizontal and the vertical axes are exchanged.

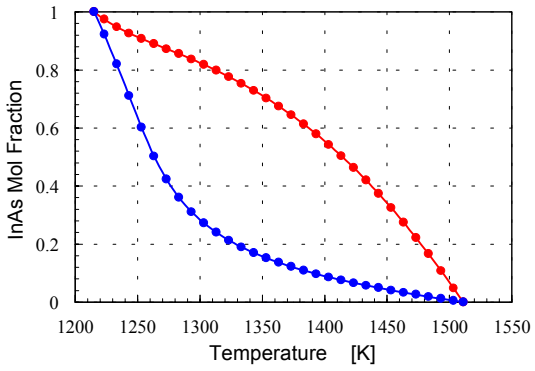

Fig. 1 Phase Diagram of InGaAs

The phase diagram is determined under the equilibrium state. Therefore, the quasi-equilibrium state is assumed in the model. If the model of the supercooling at the interface is established in future, more precise solutions will be obtained. But the current model should be reliable because the kinetics anisotropy of semiconductor crystals is not so large and the growth rate is small.

In order to solve Eqs. (1) – (8) numerically, the boundary fitted coordinate (BFC) method [3–7], which is a kind of a finite difference method, is used in this study. The BFC method solves the governing equations that are transformed from the physical space to the computational space. Therefore, curved boundaries in the physical space are transformed to linear boundaries, which are rectangular each other.

The BFC method has a feature of automatic grid generation. In this study, the method of the grid generation based on the Poisson equation is used, that is,

$$\xi_{rr} + \xi_{zz} = 0, \text{ and} \qquad (9)$$

$$\eta_{rr} + \eta_{zz} = 0, \qquad (10)$$

where ξ and η are the computational coordinates and the subscripts represent the partial differentials.

This method is well known as one of the methods of generating a smooth grid. Since Eqs. (9) and (10) are inconvenient for obtaining the *r*-*z* coordinates in the physical space, inverse expressions should be introduced. In order to invert these equations, the relationship between minute elements in both spaces is required and can be represented as

$$\begin{pmatrix} d\xi \\ d\eta \end{pmatrix} = \begin{pmatrix} \xi_r & \xi_z \\ \eta_r & \eta_z \end{pmatrix} \begin{pmatrix} dr \\ dz \end{pmatrix}, \text{ and} \tag{11}$$

$$\begin{pmatrix} dr \\ dz \end{pmatrix} = \begin{pmatrix} r_\xi & r_\eta \\ z_\xi & z_\eta \end{pmatrix} \begin{pmatrix} d\xi \\ d\eta \end{pmatrix}. \tag{12}$$

Equation (11) can be rewritten as

$$\begin{pmatrix} d\xi \\ d\eta \end{pmatrix} = \frac{1}{J} \begin{pmatrix} z_\eta & -r_\eta \\ -z_\xi & r_\xi \end{pmatrix} \begin{pmatrix} dr \\ dz \end{pmatrix}, \tag{13}$$

where J is Jacobian, $r_\xi z_\eta - r_\eta z_\xi$. By comparing Eq. (11) with Eq. (13), the relationship is obtained as follows;

$$\xi_r = \frac{z_\eta}{J}, \quad \xi_z = -\frac{r_\eta}{J},$$

$$\eta_r = -\frac{z_\xi}{J}, \quad \eta_z = \frac{r_\xi}{J}. \tag{14}$$

Basing on Eq. (14), ξ_{rr}, ξ_{zz}, η_{rr} and η_{zz} can be obtained. For example, ξ_{rr} can be represented as

$$\begin{aligned} \xi_{rr} &= \frac{\partial}{\partial r}\left(\frac{z_\eta}{J}\right) \\ &= \left(\xi_r \frac{\partial}{\partial \xi} + \eta_r \frac{\partial}{\partial \eta}\right)\left(\frac{z_\eta}{J}\right) \\ &= \xi_r \frac{\frac{\partial z_\eta}{\partial \xi} J - \frac{\partial J}{\partial \xi} z_\eta}{J^2} \\ &\quad + \eta_r \frac{\frac{\partial z_\eta}{\partial \eta} J - \frac{\partial J}{\partial \eta} z_\eta}{J^2} \end{aligned} \tag{15}$$

The first term and the second one in the right side of Eq. (15) are represented as

$$\begin{aligned} &\frac{\frac{\partial z_\eta}{\partial \xi} J - \frac{\partial J}{\partial \xi} z_\eta}{J^2} \\ &= \frac{-z_\eta{}^2 r_{\xi\xi} + z_\xi z_\eta r_{\xi\eta} - r_\eta z_\xi z_{\xi\eta} + r_\eta z_\eta z_{\xi\xi}}{J^2} \end{aligned} \tag{16}$$

and

$$\begin{aligned} &\frac{\frac{\partial z_\eta}{\partial \eta} J - \frac{\partial J}{\partial \eta} z_\eta}{J^2} \\ &= \frac{z_\xi z_\eta r_{\eta\eta} - z_\eta{}^2 r_{\xi\eta} + r_\eta z_\eta z_{\xi\eta} - r_\eta z_\xi z_{\eta\eta}}{J^2} \end{aligned}, \tag{17}$$

respectively. Equations (16) and (17) are substituted to Eq. (15) and thus the equation is rewritten as follows;

$$\begin{aligned} &\xi_{rr} \\ &= \frac{1}{J^3}\left[-z_\eta \left(z_\eta{}^2 r_{\xi\xi} - 2 z_\xi z_\eta r_{\xi\eta} + z_\xi{}^2 r_{\eta\eta}\right).\right. \\ &\left. + r_\eta \left(z_\eta{}^2 z_{\xi\xi} - 2 z_\xi z_\eta z_{\xi\eta} + z_\xi{}^2 z_{\eta\eta}\right)\right] \end{aligned} \tag{18}$$

By the same way, ξ_{zz} can be obtained as

$$\xi_{zz} = \frac{1}{J^3}\left[-z_\eta\left(r_\eta{}^2\, r_{\xi\xi} - 2\, r_\xi\, r_\eta\, r_{\xi\eta} + r_\xi{}^2\, r_{\eta\eta}\right)\right. \\ \left. + r_\eta\left(r_\eta{}^2\, z_{\xi\xi} - 2\, r_\xi\, r_\eta\, z_{\xi\eta} + r_\xi{}^2\, z_{\eta\eta}\right)\right] \qquad (19)$$

Equations (18) and (19) are substituted to Eq. (9) and then,

$$\xi_{rr} + \xi_{zz} \\ = \frac{1}{J^3}\left[-z_\eta\left(\alpha\, r_{\xi\xi} - 2\,\beta\, r_{\xi\eta} + \gamma\, r_{\eta\eta}\right)\right. \\ \left. + r_\eta\left(\alpha\, z_{\xi\xi} - 2\,\beta\, z_{\xi\eta} + \gamma\, z_{\eta\eta}\right)\right] = 0 \qquad (20)$$

is obtained. Equation (10) is rewritten by using the same transformation method as

$$\eta_{rr} + \eta_{zz} \\ = \frac{1}{J^3}\left[z_\xi\left(\alpha\, r_{\xi\xi} - 2\,\beta\, r_{\xi\eta} + \gamma\, r_{\eta\eta}\right),\right. \\ \left. - r_\xi\left(\alpha\, z_{\xi\xi} - 2\,\beta\, z_{\xi\eta} + \gamma\, z_{\eta\eta}\right)\right] = 0 \qquad (21)$$

where

$$\alpha = r_\eta^2 + z_\eta^2, \quad \beta = r_\xi\, r_\eta + z_\xi\, z_\eta, \text{ and}$$

$$\gamma = r_\xi^2 + z_\xi^2. \qquad (22)$$

By solving Eqs. (20) and (21) simultaneously, the following equations are obtained;

$$\alpha\, r_{\xi\xi} - 2\,\beta\, r_{\xi\eta} + \gamma\, r_{\eta\eta} = 0, \text{ and} \qquad (23)$$

$$\alpha\, z_{\xi\xi} - 2\,\beta\, z_{\xi\eta} + \gamma\, z_{\eta\eta} = 0. \qquad (24)$$

By solving these equations, the coordinates of the nodes in the physical space can be obtained.

The partial differentials by the component corresponding to the physical coordinates, *r* and *z*, can be also expressed by using Eq. (14), that is,

$$\frac{\partial}{\partial r} = \frac{z_\eta}{J}\frac{\partial}{\partial \xi} - \frac{z_\xi}{J}\frac{\partial}{\partial \eta}, \qquad (25)$$

$$\frac{\partial}{\partial z} = -\frac{r_\eta}{J}\frac{\partial}{\partial \xi} + \frac{r_\xi}{J}\frac{\partial}{\partial \eta}, \qquad (26)$$

$$\frac{\partial^2}{\partial r^2} \\ = \frac{1}{J^2}\left(z_\eta{}^2\,\frac{\partial^2}{\partial \xi^2}\right. \\ \left. - 2\, z_\xi\, z_\eta\,\frac{\partial^2}{\partial \xi\,\partial \eta} + z_\xi{}^2\,\frac{\partial^2}{\partial \eta^2}\right) \\ + \xi_{rr}\,\frac{\partial}{\partial \xi} + \eta_{rr}\,\frac{\partial}{\partial \eta}, \text{ and} \qquad (27)$$

$$\frac{\partial^2}{\partial z^2} \\ = \frac{1}{J^2}\left(r_\eta{}^2\,\frac{\partial^2}{\partial \xi^2} - 2\, r_\xi\, r_\eta\,\frac{\partial^2}{\partial \xi\,\partial \eta}\right. \\ \left. + r_\xi{}^2\,\frac{\partial^2}{\partial \eta^2}\right) \\ + \xi_{zz}\,\frac{\partial}{\partial \xi} + \eta_{zz}\,\frac{\partial}{\partial \eta}. \qquad (28)$$

By using Eqs. (25) – (28), all the governing equations in the physical space can be transformed to the equations in the computational space. Before the physical coordinates are transformed to the computational coordinates, Eqs. (5) and (6) must be transformed to the scalar expression. In this transformation, it is assumed that the interface shape and its location can be expressed by using any function *f*, that is,

$$z = f(r, t). \qquad (29)$$

By using Eq. (29), the normal unit vector $\hat{\boldsymbol{n}}$ can be described as

$$\hat{\boldsymbol{n}} = \frac{1}{\sqrt{1+\left(\frac{\partial f}{\partial r}\right)^2}}\left(-\frac{\partial f}{\partial r}, 1\right). \qquad (30)$$

This equation is substituted to the right side of Eq. (5);

$$\begin{aligned}&\text{(Right Side)}\\ &\equiv -\kappa_L (\nabla T)_L \cdot \hat{\boldsymbol{n}} + \kappa_S (\nabla T)_S \cdot \hat{\boldsymbol{n}}\\ &= \frac{1}{\sqrt{1+\left(\frac{\partial f}{\partial r}\right)^2}}\left\{-\kappa_L\left(\frac{\partial T}{\partial z}-\frac{\partial T}{\partial r}\frac{\partial f}{\partial r}\right)\right.\\ &\left.+\kappa_S\left(\frac{\partial T}{\partial z}-\frac{\partial T}{\partial r}\frac{\partial f}{\partial r}\right)\right\}\end{aligned} \qquad (31)$$

On the other hand, the left side of Eq. (5) is represented as;

$$\text{(Left Side)} = \frac{L_{SL}\,\rho}{\sqrt{1+\left(\frac{\partial f}{\partial r}\right)^2}}\frac{\partial f}{\partial t}. \qquad (32)$$

By combining Eqs. (31) and (32), Eq. (5) can be expressed as

$$\begin{aligned}L_{SL}\,\rho\frac{\partial f}{\partial t} = &\left\{-\kappa_L\left(\frac{\partial T}{\partial z}-\frac{\partial T}{\partial r}\frac{\partial f}{\partial r}\right)_L\right.\\ &\left.+\kappa_S\left(\frac{\partial T}{\partial z}-\frac{\partial T}{\partial r}\frac{\partial f}{\partial r}\right)_S\right\}\end{aligned}. \qquad (33)$$

By using the same transformation, Eq. (6) can be also expressed as

$$\left(C_L - C_S\right)\frac{\partial f}{\partial t} = -D_L\left(\frac{\partial C}{\partial z}-\frac{\partial C}{\partial r}\frac{\partial f}{\partial r}\right)_L. \qquad (34)$$

The governing equations, Eqs. (1) – (4), (33) and (34) are transformed from the physical coordinates, r and z, to the computational coordinates, ξ and η. In the transformation, the time differential of the following expression is used;

$$\begin{aligned}\frac{\partial}{\partial t} = &\frac{\partial}{\partial t'} - \frac{1}{J}\left(z_\eta\frac{\partial}{\partial \xi} - z_\xi\frac{\partial}{\partial \eta}\right)\frac{\partial r}{\partial t'}\\ &-\frac{1}{J}\left(-r_\eta\frac{\partial}{\partial \xi} + r_\xi\frac{\partial}{\partial \eta}\right)\frac{\partial z}{\partial t'}\end{aligned}. \qquad (35)$$

Since t' is actually equal value to t, t' is replaced with t after here.

By substituting Eqs. (25) – (28) and (35) to the governing equations, the transformed expression can be obtained. The energy transport equation, the mass transport equation, the vorticity transport equation, the stream function equation, the energy balance equation and the mass balance equation are described as follows, respectively;

$$\begin{aligned}&\rho\, C_p\left\{\frac{\partial T}{\partial t} - \frac{1}{J}\left(z_\eta T_\xi - z_\xi T_\eta\right)\frac{\partial r}{\partial t}\right.\\ &\left.-\frac{1}{J}\left(-r_\eta T_\xi + r_\xi T_\eta\right)\frac{\partial z}{\partial t}\right\}\\ &-\rho\, C_p\frac{1}{r}\frac{1}{J}\left(\psi_\xi T_\eta - \psi_\eta T_\xi\right),\\ &= \kappa\frac{1}{J^2}\left(\alpha T_{\xi\xi} - 2\beta T_{\xi\eta} + \gamma T_{\eta\eta}\right)\\ &+\kappa\frac{1}{r}\frac{1}{J}\left(z_\eta T_\xi - z_\xi T_\eta\right)\end{aligned} \qquad (36)$$

$$\begin{aligned}&\frac{\partial C_L}{\partial t} - \frac{1}{J}\left(z_\eta C_{L\xi} - z_\xi C_{L\eta}\right)\frac{\partial r}{\partial t}\\ &-\frac{1}{J}\left(-r_\eta C_{L\xi} + r_\xi C_{L\eta}\right)\frac{\partial z}{\partial t}\\ &-\frac{1}{r}\frac{1}{J}\left(\psi_\xi C_{L\eta} - \psi_\eta C_{L\xi}\right),\\ &= D_L\frac{1}{J^2}\left(\alpha C_{L\xi\xi} - 2\beta C_{L\xi\eta} + \gamma C_{L\eta\eta}\right)\\ &+D_L\frac{1}{r}\frac{1}{J}\left(z_\eta C_{L\xi} - z_\xi C_{L\eta}\right)\end{aligned} \qquad (37)$$

$$\frac{\partial C_S}{\partial t}-\frac{1}{J}\left(z_\eta C_{S\xi}-z_\xi C_{S\eta}\right)\frac{\partial r}{\partial t} -\frac{1}{J}\left(-r_\eta C_{S\xi}+r_\xi C_{S\eta}\right)\frac{\partial z}{\partial t} = D_S\frac{1}{J^2}\left(\alpha C_{S\xi\xi}-2\beta C_{S\xi\eta}+\gamma C_{S\eta\eta}\right) +D_S\frac{1}{r}\frac{1}{J}\left(z_\eta C_{S\xi}-z_\xi C_{S\eta}\right) \quad (38)$$

$$\begin{aligned}&\frac{\partial \omega}{\partial t}-\frac{1}{J}\left(z_\eta \omega_\xi-z_\xi \omega_\eta\right)\frac{\partial r}{\partial t} -\frac{1}{J}\left(r_\eta \omega_\xi-r_\xi \omega_\eta\right)\frac{\partial z}{\partial t} +\frac{1}{r}\frac{1}{J^2}\left(-r_\eta \psi_\xi+r_\xi \psi_\eta\right)\cdot\left(z_\eta \omega_\xi-z_\xi \omega_\eta\right) -\frac{1}{r}\frac{1}{J^2}\left(z_\eta \psi_\xi-z_\xi \psi_\eta\right)\cdot\left(-r_\eta \omega_\xi+r_\xi \omega_\eta\right) -\frac{1}{r^2}\frac{1}{J}\omega\left(-r_\eta \psi_\xi+r_\xi \psi_\eta\right)\\ &=\nu\frac{1}{J^2}\left(\alpha \omega_{\xi\xi}-2\beta \omega_{\xi\eta}+\gamma \omega_{\eta\eta}\right) +\nu\frac{1}{r}\frac{1}{J}\left(z_\eta \omega_\xi-z_\xi \omega_\eta\right) -\nu\frac{1}{r^2}\omega +\frac{1}{J}B g\left(z_\eta T_\xi-z_\xi T_\eta\right) +\frac{1}{J}G g\left(z_\eta C_\xi-z_\xi C_\eta\right)\end{aligned} \quad (39)$$

$$\begin{aligned}&-r J^2\omega\\ &=\alpha\psi_{\xi\xi}-2\beta\psi_{\xi\eta}+\gamma\psi_{\eta\eta} -\frac{J}{r}\left(z_\eta \psi_\xi-z_\xi \psi_\eta\right)\end{aligned} \quad (40)$$

$$\begin{aligned}&L_{SL}\rho\frac{\partial f}{\partial t}\\ &=-\kappa_L\frac{1}{r_\xi}\frac{1}{J_L}\left(-\beta T_\xi+\gamma T_\eta\right)_L +\kappa_S\frac{1}{r_\xi}\frac{1}{J_S}\left(-\beta T_\xi+\gamma T_\eta\right)_S\end{aligned} \quad (41)$$

$$\begin{aligned}&\left(C_L-C_S\right)\frac{\partial f}{\partial t}\\ &=-D_L\frac{1}{r_\xi}\frac{1}{J_L}\left(-\beta C_{L\xi}+\gamma C_{L\eta}\right)_L\end{aligned} \quad (42)$$

where subscripts of L and S represent liquid phase and solid phase, respectively. The method of obtaining solutions is summarized and shown in Fig. 2.

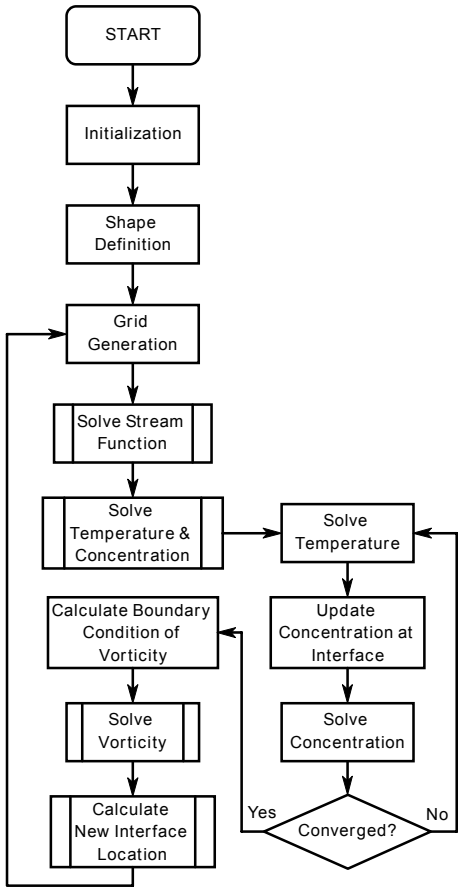

Fig. 2 Flow Chart

Calculation Results

In order to generate a grid, Eqs. (23) and (24) are applied to a cartridge shown in Fig. 3. The cartridge, which was designed last year [8], is the present candidate for a flight experiment. The cartridge is designed so as to obtain a convex shape, which contributes to prevent polycrystallization. Since the numerical analysis, which performed last year, did not include the mass transport and was modeled as the Bridgeman method, however, it is not clear that the configuration is also suitable for the

TLZ method. Therefore, the analysis has the role of the performance investigation in the case of the TLZ method. It is planned to revise the cartridge configurations next year based on the calculation results.

The generated grid is shown in Fig. 4. In the figure, the shape of the cartridge is plotted as orange solid lines. By using the grid, temperature, concentration, stream function, and vorticity distributions are calculated. The heating sequence is as follows; (i) melting back with heater speed of 5 mm/hr for 4 hours, (ii) stopping heater transfer for 1 hour, (iii) growing a crystal with heater speed of 0.5 mm/hr. The temperature profile is given on the surface. It is assumed that the profile moves with the same speed as the heater transfer speed. The temperature profile is a combination of linear temperature profile with temperature gradients of 20 K/cm and 80 K/cm. The temperature is clipped so as to be a certain temperature range, 313 K to 1573 K. The end surface at the higher temperature side is assumed to be adiabatic. The end surface at the lower temperature side is well cooled and thus the temperature at this side is assumed to be equal to the temperature on the surface. The gravity direction is from the higher temperature side to the lower one along the axis. The governing equations are transformed to the implicit difference equations and solved by the successive overrelaxation (SOR) method. The used thermophysical properties are summarized in Tables 1 and 2.

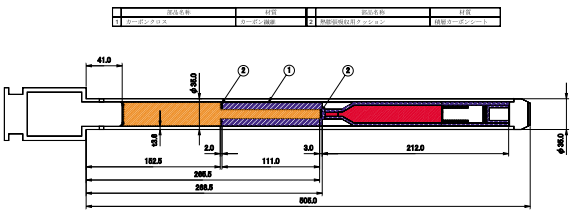

Fig. 3 Schematic View of a Cartridge

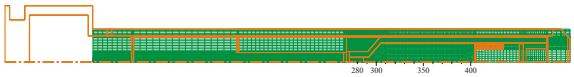

Fig. 4 Generated Grids

Table 1 Thermophysical Properties of InGaAs

Coefficient of Volume Expansion β [1/K]	1.83×10^{-4} (GaAs)
Kinetic Viscosity ν [m^2/s]	3.0×10^{-7}
Density ρ [kg/m^3]	ρ_L=5.9×10^{3} (1296 K) ρ_S=5.3×10^{3} (1296 K)
Viscosity $\mu=\nu\cdot\rho$ [Pa·s]	1.8×10^{-3}
Specific Heat C_p [J/(kg·K)]	3.2×10^{2} (1296 K)
Thermal Conductivity κ [W/(m·K)]	κ_L=3.0 (1296 K) κ_S=1.2 (1296 K)
Themal Diffusivity $\alpha=\kappa/(\rho\cdot C_p)$ [m^2/s]	α_L= 1.6×10^{-6} (1296 K) α_S= 7.1×10^{-7} (1296 K)
Diffusion Coefficent D [m^2/s]	D_L= 1.0×10^{-8} D_S= 1.0×10^{-11}
Latent Heat L_{SL} [J/kg]	5.0×10^{5}

Table 2 Typical Thermophysical Properties

Material	Thermal Conductivity κ [W/(m·K)]	Density ρ [kg/m^3]	Specific Heat C_p [J/(kg·K)]
Ta	60.2	16.36×10^{3}	1.54×10^{2}
WC-103	38.1 (1144 K) 40.7 (1386 K)	8.85×10^{3}	3.43×10^{2}
Cu	3.5×10^{2}	8.96×10^{3}	5.0×10^{2}
Fused Crystal	4.0	2.2×10^{3}	1.13×10^{3}
BN / pBN	7.0	2.0×10^{3} (BN) 2.1×10^{3} (pBN)	2.1×10^{3}
Carbon Cloth / Laminated Carbon Sheet	5.0	1.0×10^{3}	1.68×10^{3}
Graphite Spring	44.0	1.7×10^{3}	1.68×10^{3}
Arsenic Vapor (1 atm)	1.58×10^{-3}	1.45	1.0×10^{3}
Vacuum (~ 10^{-5} Torr)	9.2×10^{-11}	3.7×10^{-10}	1.01×10^{3}

In order to understand the TLZ method, typical results of a temperature distribution, a concentration distribution, a flow pattern, and degree of supercooling, and time evolutions of an interface shape, a growth rate, zone width under various gravity levels are investigated. Figure 5 and 6 show the typical calculation results of the temperature distribution and flow patterns around the zone, respectively. In both figures, the left side is the seed side and the right the feed side. The black lines

represent the solid-liquid interfaces. The zone is formed between the interfaces. Unfortunately, the temperature distribution has the radial dependency, which means that it is difficult to regard the distribution as being one-dimensional. This is consistent with the general heat flux flow in the case of the ohmic heating furnace such as Gradient Heating Furnace (GHF). Namely, the heat flux is incoming to the cartridge surface at the higher temperature side, goes along the axis around the middle, and is outgoing from the cartridge surface at the lower temperature side. Although the heat sink is installed in the cartridge in order to weaken this tendency, it is essentially impossible to achieve the radial uniformity of the temperature distribution. But the radial temperature gradient may be able to be negligibly small as compared with the axial one, for example, a sample with smaller radius is used. The feasibility of obtaining the smaller radial temperature gradient will be investigated next year as a part of the revision of the cartridge configuration.

At the lower gravity of less than about 10^{-4} *g*, the flow patterns are laminar. As the gravity increases, the pattern becomes more complicated. But the effect of the convection on the temperature distribution can be clearly observed only at 1 *g*. This is because the Prandtle Number is very small. In the TLZ method, the gravity of less than or equal to 10^{-1} *g* is enough to achieve the thermally diffusion-dominant condition.

The center of the vortex is located around the middle of the zone under the low gravity conditions. Increasing the gravity level, the center moves towards the feed side. Therefore, the disturbance by the convection at the feed side will be stronger than that at the seed side. This may be suitable for the prevention of the surface roughening at the growth interface. But the strong interface deformation at the feed side may occur. This may be one of the mechanisms of the failure of the TLZ mode because the TLZ mode has a limitation on the zone width. Further investigations should be required.

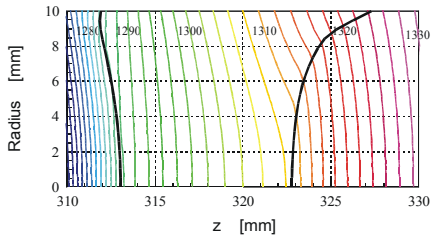

(a) 0 *g*

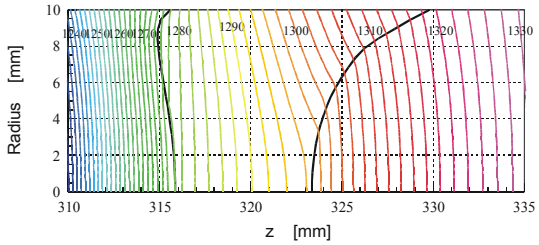

(b) 10^{-5} *g*

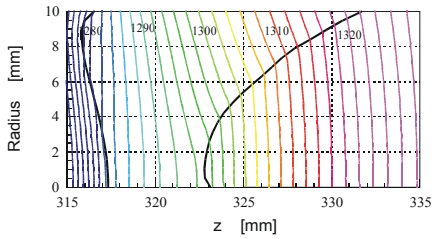

(c) 10^{-4} *g*

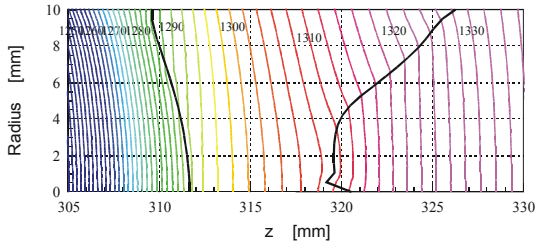

(d) 10^{-2} *g*

Fig. 5 Typical Temperature Distributions around Solution Zone (*Cont.*)

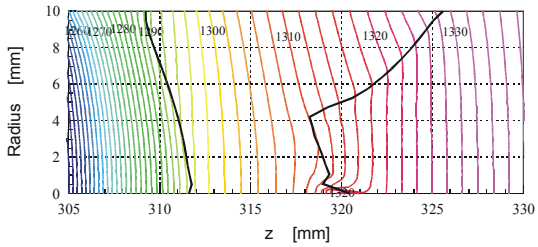

(e) 10^{-1} *g*

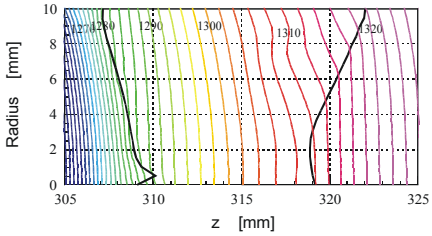

(f) 1 *g*

Fig. 5 Typical Temperature Distributions around Solution Zone

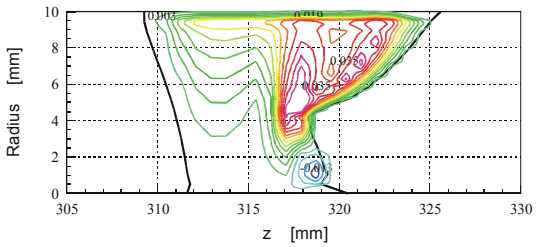

(d) 10^{-1} *g*

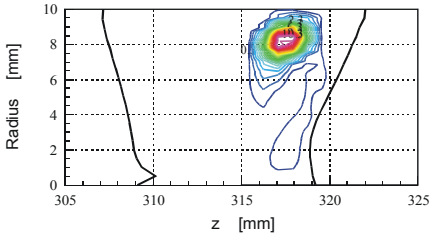

(e) 1 *g*

Fig. 6 Typical Flow Patterns in Solution Zone

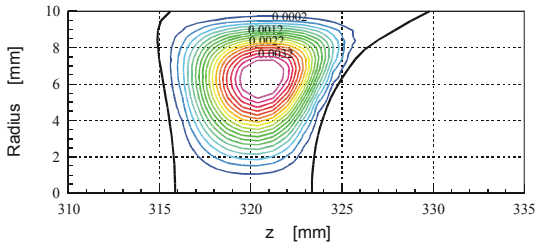

(a) 10^{-5} *g*

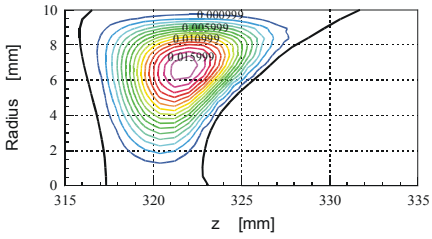

(b) 10^{-4} *g*

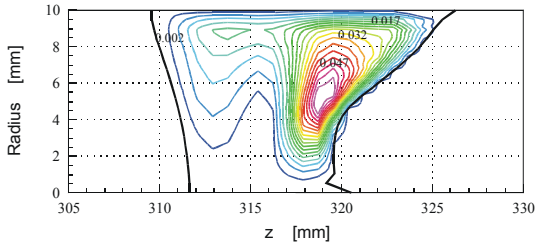

(c) 10^{-2} *g*

The TLZ method is one of the solution growths. Since the solute diffusion coefficient is much smaller than the thermal diffusion coefficient, the solute transport is generally much sensitive to the convection as compared with the thermal transport. The numerical code can calculate the concentration distributions and the calculation results are shown in Fig. 7. In the case of the gravity level of less than or equal to 10^{-5} *g*, the volume-averaged mass flux by the diffusion is larger than that by the convection by about 70 %, that is, 1.9×10^{-4} mm/s and 1.1×10^{-4} mm/s, respectively, where the concentration is normalized and dimensionless. On the other hand, in the case of 10^{-4} *g*, the flux by the convection is larger than that by the diffusion by about 400 %, that is, 4.1×10^{-4} mm/s and 8.2×10^{-5} mm/s. Although the absolute value of the diffusion flux in the case of 10^{-4} *g* is different from the value in the case of 10^{-5} *g*, the value depends on the time and the concentration distribution. Since the convection flow pattern and the flow velocity affect the concentration distribution, the absolute value difference should mean the change of the convection

strength. From these results, the gravity of 10^{-5} g at least is required in order to achieve the diffusion-dominant condition. But in other gravity cases, the solute distribution is not so drastically affected by the convection in the cases of the gravity of less than or equal to 10^{-1} g. This is one of the features of the TLZ method, that is, the solute distribution is also robust against the convection.

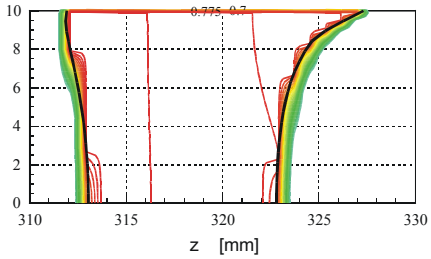

(a) 0 g

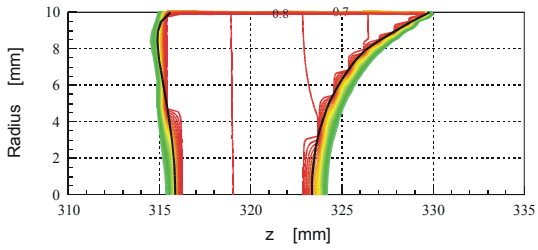

(a) 10^{-5} g

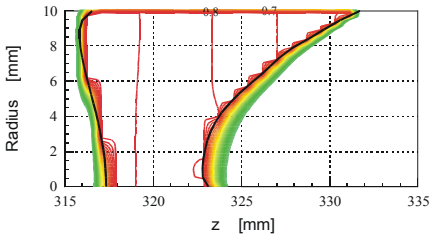

(c) 10^{-4} g

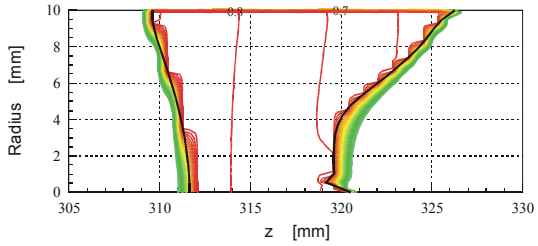

(d) 10^{-2} g

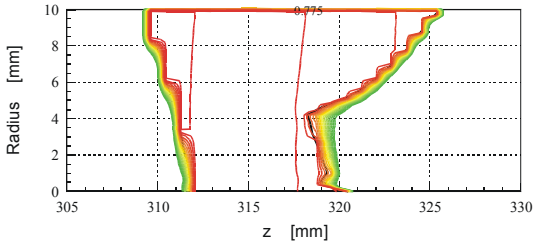

(e) 10^{-1} g

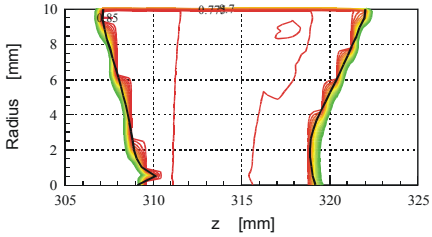

(f) 1 g

Fig. 7 Solute Distributions in Solution Zone

The time evolutions of the interface shapes are investigated. The shape is generally important to obtain a single crystal. In addition, the shape change means that the zone-width depends on radial position. This may cause the breakdown of the TLZ mode.

The shapes at seed side under various gravity levels are shown in Fig. 8. In this figure, the red lines are plotted every 2 hours, and the blue ones are plotted every 30 minutes or 1 hour. The left side is the seed side and the right side is the melt side. At low gravity levels, the shape is convex towards the solvent zone at the initial stage, and then the shape changes to weak W-shape gradually.

Unfortunately, at high gravity levels, the calculation is easily unstable due to the influence of the stronger convection. In order to solve the numerical instability problem fundamentally, more nodes and a smaller time step should be required. But the fundamental solution takes much longer time to obtain a result. Therefore, in this study, a result at lower gravity is used as an initial condition at higher gravity to reduce the numerical instability. This

way takes shorter time, but the accuracy becomes worse. The accumulation of the numerical error will bring to calculation failure at some time. But this is enough to understand the tendency of the interface shape or to understand the differences of the typical results such as flow patterns among the various gravity levels. At the seed side, the influence of the numerical error accumulation can be observed around the axis in Fig. 8 (e) and (f).

If a large amount of CPU time to perform more precise calculation can be provided, a large-scale calculation may be executed. But the priority is low because the understanding of the tendency or the behavior of the interface shape, the concentration distribution, the temperature distribution, the flow pattern or any information to determine the cartridge configuration is much more important.

Figure 8 shows that the crystal growth occurs spontaneously even though the heater translation direction is opposite to the growth direction, i.e. a back-melt phase. This is one of the major features of the TLZ method. The situation at the feed side is very similar to that at the seed side, namely, spontaneous dissolution occurs as shown in Fig. 9. In this figure, the red lines are plotted every 2 hours, and the blue ones are plotted every 30 minutes or 1 hour. The left side is the melt side and the right side is the feed side. Although in Fig. 9 (d), (e) and (f), the numerical instability around the axis can also be observed, the tendency is sufficiently understandable.

In order to grow a homogeneous crystal, the flat interface shape is the best, but such shape is the most difficult to achieve. The better shape, which is easier to realize, is convex towards melt. At both the seed side and the feed side, such shape can be satisfied. Namely, one of the important requirements for the single crystal growth can be satisfied.

The interface shape at the feed side is much more deformed as compared with the shape at the seed side. This tendency is consistent with the ground-based experimental data. So the calculation may be helpful to discuss the experimental conditions not only in space but also on the earth.

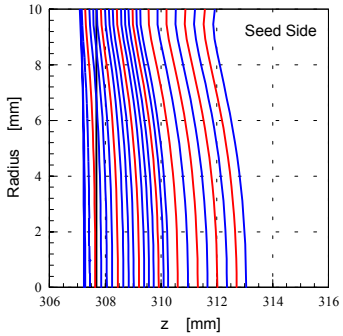

(a) 0 *g*

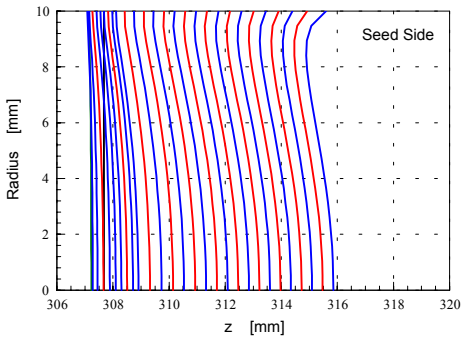

(b) 10^{-5} *g*

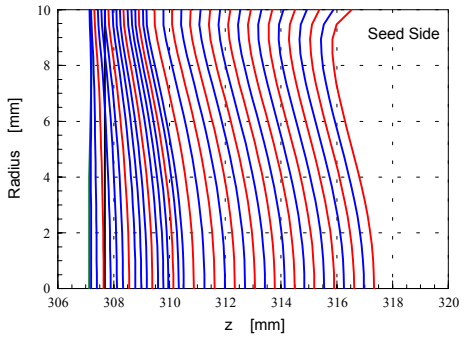

(c) 10^{-4} *g*

Fig. 8 Time Evolutions of Interface Shapes at Seed Side (Red Line: Every 2 Hours) (*Cont.*)

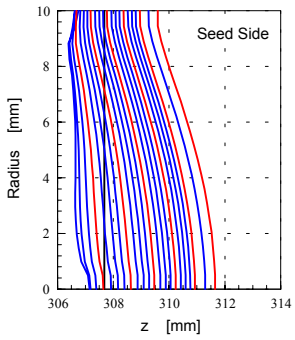

(d) 10^{-2} g

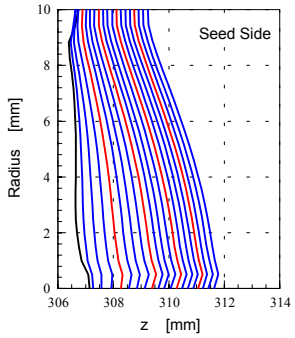

(e) 10^{-1} g

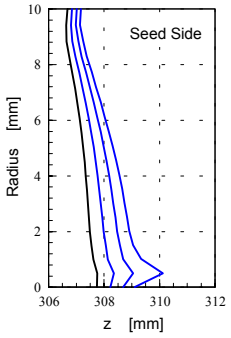

(f) 1 g

Fig. 8 Time Evolutions of Interface Shapes at Seed Side (Red Line: Every 2 Hours)

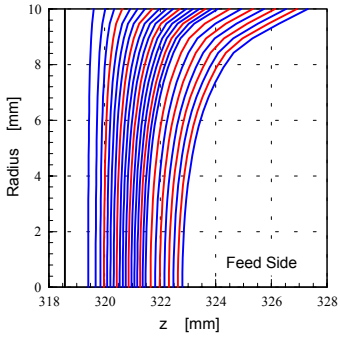

(a) 0 g

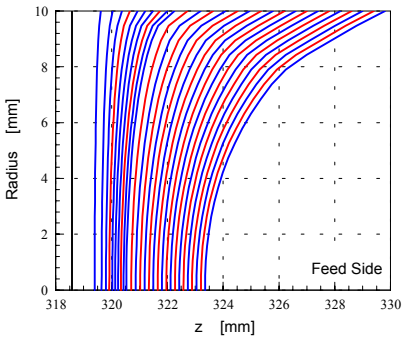

(b) 10^{-5} g

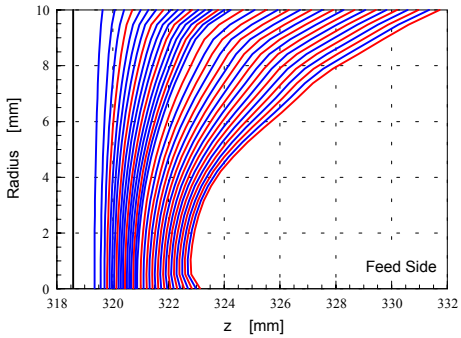

(c) 10^{-4} g

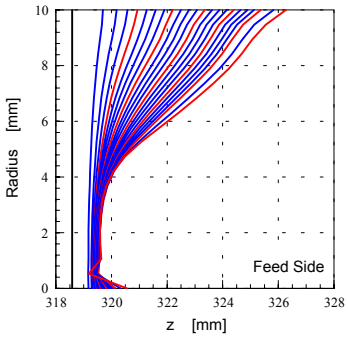

(d) 10^{-2} g

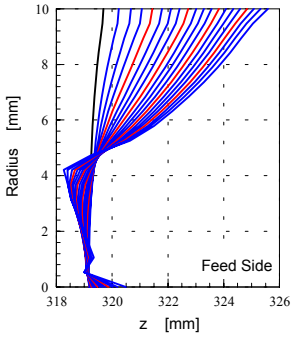

(e) 10^{-1} g

Fig. 9 Time Evolutions of Interface Shapes at Feed Side (Red Line: Every 2 Hours) (*Cont.*)

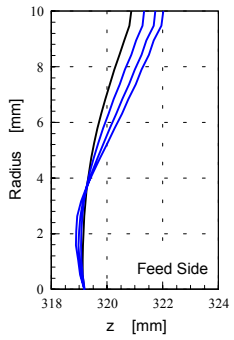

(f) 1 *g*

Fig. 9 Time Evolutions of Interface Shapes at Feed Side (Red Line: Every 2 Hours)

In order to obtain a single crystal, it is important that not only the interface shape but also the degree of supercooling. Therefore, the degree of the supercooling is investigated and is shown in Fig. 10. In 0 *g* case, the supercooling region can hardly be observed. As the gravity increases, however, the supercooling region occurs around the axis. In the current boundary conditions, the maximum supercooling location is near the feed on axis. Although the allowable value of the supercooling is unknown now, if the degree of the supercooling of less than 0.1 % is assumed to be allowable, the gravity of less than or equal to 10^{-4} *g* is required. This gravity should be easily achieved by the International Space Station. The degree of supercooling becomes maximal at 1 *g* , but the value is only about 0.48 %. This is not so large value and may be allowable for suppression of excess nucleation. These results suggests that the current boundary conditions such as the heating condition and the gravity direction are suitable for the suppression of the supercooling.

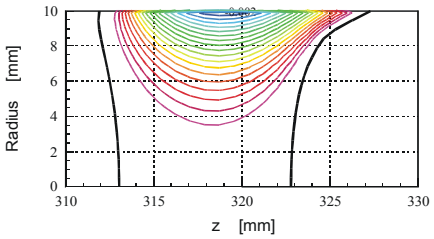

(a) 0 *g*

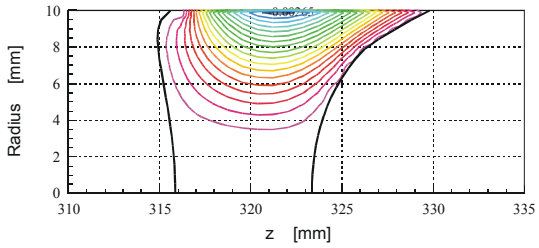

(b) 10^{-5} *g*

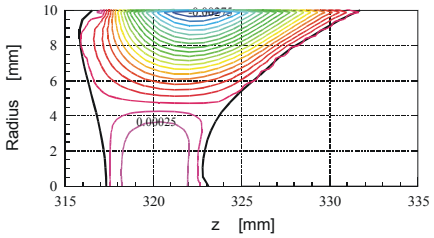

(c) 10^{-4} *g*

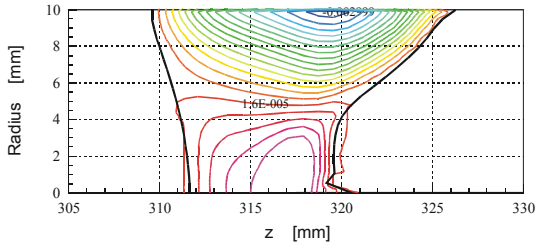

(d) 10^{-2} *g*

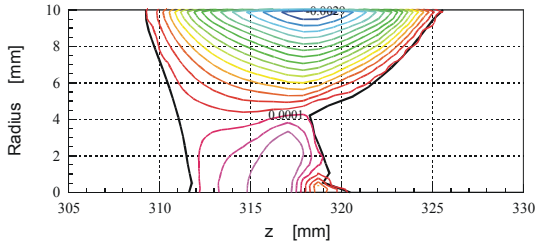

(e) 10^{-1} *g*

Fig. 10 Distribution of Degree of Supercooling (*Cont.*)

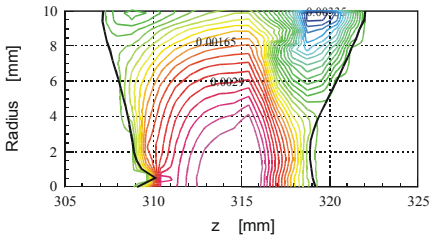

(f) 1 *g*

Fig. 10 Distribution of Degree of Supercooling

Discussion

The TLZ method has several superiorities as compared with conventional growth methods, that is, (i) spontaneous growth, (ii) robustness against the convection. But there may be limitations for obtaining large and homogeneous crystals. One of the limitations may be the maintenance of the zone width. The zone width may disappear or stretch resulting in the breakdown of the TLZ mode. Figure 11 shows the time evolutions of the zone widths at various gravity levels. In the cases of the low gravity of less than or equal to10^{-4} *g*, the width on axis linearly decreases though the width on the wall increases. By extrapolating the data, the time when the zone disappears on axis can be estimated; (a) 4500 min., (b) 3300 min., and (c) 3060 min. depending on gravity level. This disappearance is essential to the TLZ method because the crystal grows as indium in the zone is consumed. The disappearance also means that the growth rate is not the same as the dissolution rate. Namely, the rates are determined independently by satisfying the heat and mass balances at each interface. But the interfaces move just like the synchronized motion as a result. Of course, the time for the zone disappearance depends on the several conditions such as the interface shape, the temperature and the concentration gradients, and the gravity.

In the cases of higher gravity of more than or equal to 10^{-2} *g*, the behavior is different from the lower gravity cases, that is, the width on axis decreases but the decreasing rate also gradually becomes low, and begins to increase at a certain time. This should be caused by the convection. If this tendency is maintained, the width continues expanding and thus the TLZ mode will fail soon or later. This failure mode may be corresponding to experimental results of the extreme deformation of the interface shape at the feed side.

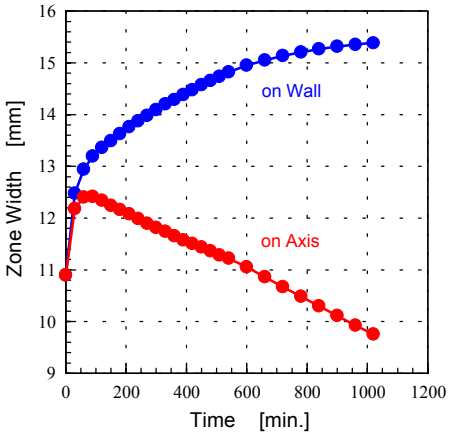

(a) 0 *g*

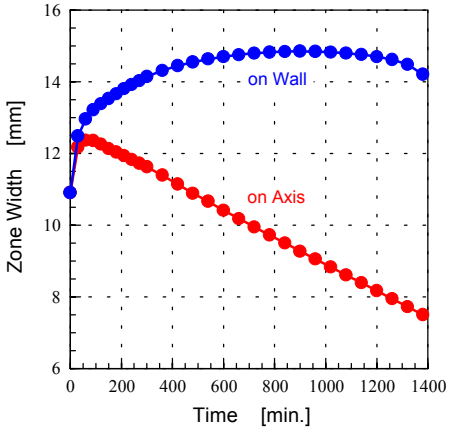

(b) 10^{-5} *g*

Fig. 11 Time Evolutions of Zone Width (*Cont.*)

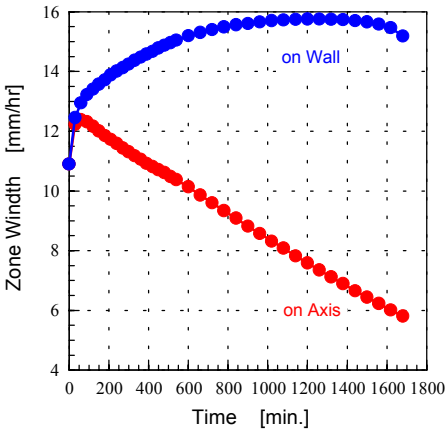

(c) 10^{-4} *g*

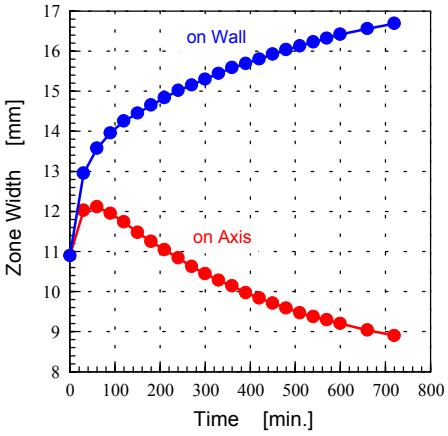

(d) 10^{-2} *g*

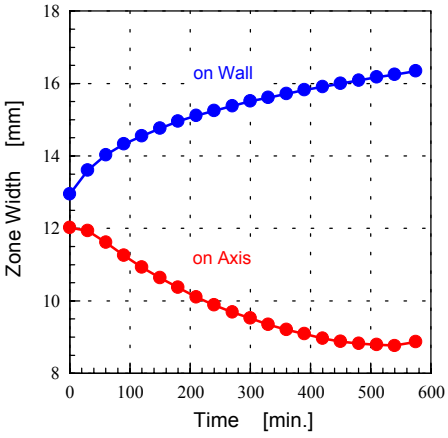

(e) 10^{-1} *g*

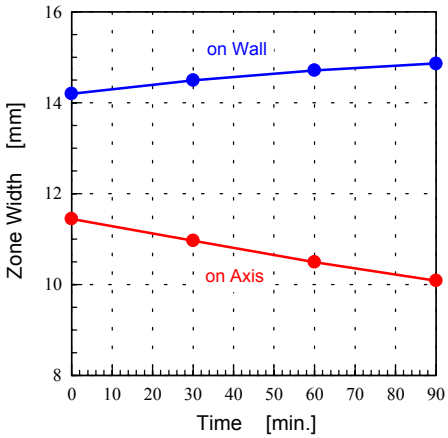

(f) 1 *g*

Fig. 11 Time Evolutions of Zone Width

In order to understand the reason of the behavior difference between at the lower gravities and the higher gravities, the time evolutions of the growth rates are investigated because the width is the result of the change of the growth rate at the seed side and the melting rate at the feed side. These are shown in Fig. 12 and 13. In Fig. 12, the growth rate on axis is nearly constant at the quasi-steady state, that is, 0.36 ± 0.02 mm/hr. The growth rate on the wall is similar to the rate on axis but the quasi-steady state may not be achieved in some cases. For short duration of several hundred minutes, the rate on the wall seems to be steady, but such condition is sometimes broken down. This is not due to the convection because the breakdown can be observed under the lower gravity conditions. Unfortunately the exact reason is not clear, but it should be sure that the width on the wall would not continue spreading under the lower gravity condition, and this should contribute to the sustenance of the TLZ mode.

In Fig. 13, the steady state is also obtained at the lower gravity levels. But the rate at the feed side is smaller than that at the seed side. This is the reason for the width decreasing on axis. The rate at the higher gravity is more difficult to reach the steady

state. The required time to become steady should be longer than the time in the lower gravity case at least. This is also caused by the convection. Since the center of the vortex is nearer the feed side than the seed side in the case of less than or equal to 10^{-2} *g*, the convection influence is larger and thus the required time to be steady becomes longer.

By using the typical growth rate and the termination time of the TLZ mode, the growth length can be obtained. The maximum length should be 27 mm at 0 *g*, 19.8 mm at 10^{-5} *g* and 18.4 mm at 10^{-4} *g* under the current boundary conditions. Though this is not so long at the point of view of the absolute value, it is long enough to evaluate the crystal quality and to make a test device of a laser diode. Of course, the maximum length can be easily longer by using the wider solution zone such as the initial value of 15 mm or 20 mm. Although the wider zone makes the maintenance of the TLZ mode more difficult, the microgravity condition will enhances the maintenance capability. In addition, another condition such as a smaller radius sample will also contribute to the longer lifetime of the TLZ mode due to the smaller deformation of the interface shape.

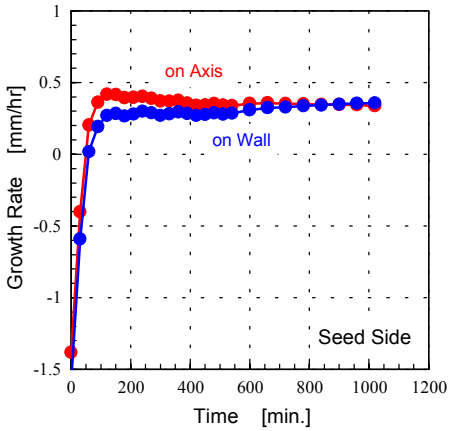

(a) 0 *g*

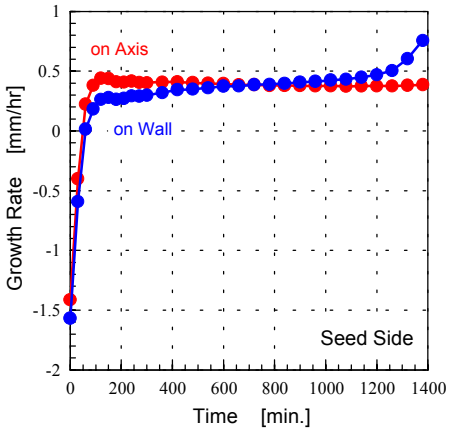

(b) 10^{-5} *g*

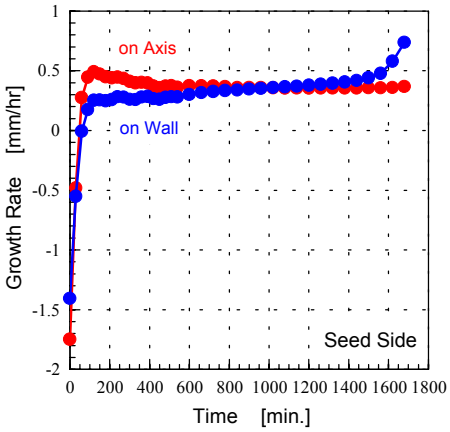

(c) 10^{-4} *g*

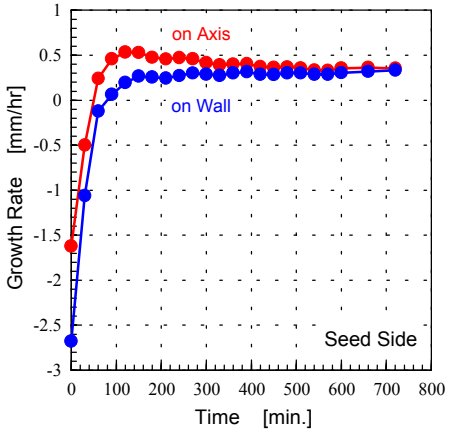

(d) 10^{-2} *g*

Fig. 12 Time Evolutions of Growth Rate at Seed Side (*Cont.*)

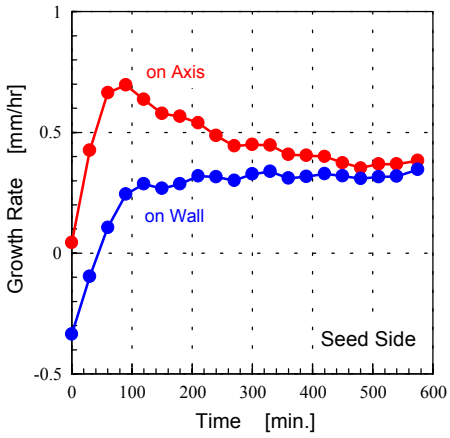

(e) 10^{-1} *g*

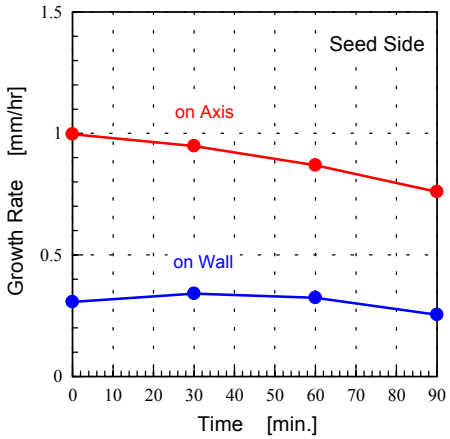

(f) 1 *g*

Fig. 12 Time Evolutions of Growth Rate at Seed Side

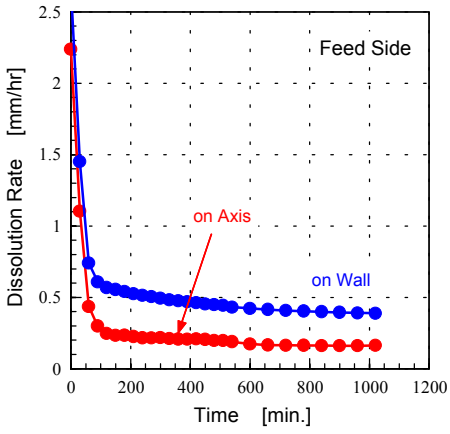

(a) 0 *g*

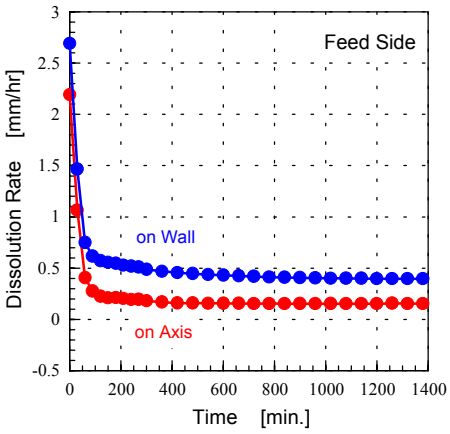

(b) 10^{-5} *g*

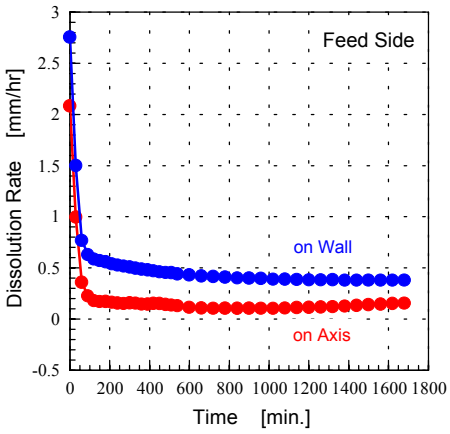

(c) 10^{-4} *g*

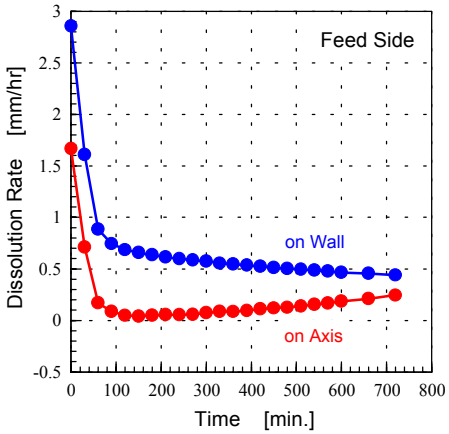

(d) 10^{-2} *g*

Fig. 13 Time Evolutions of Dissolution Rate at Feed Side (*Cont.*)

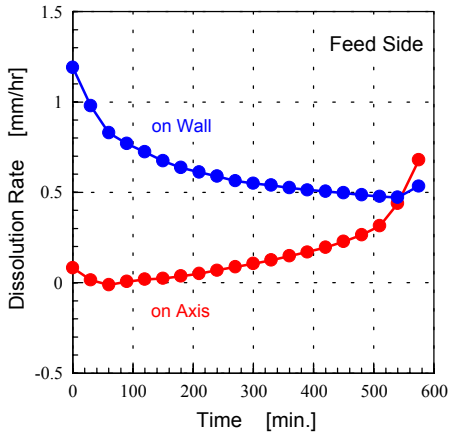

(e) 10^{-1} *g*

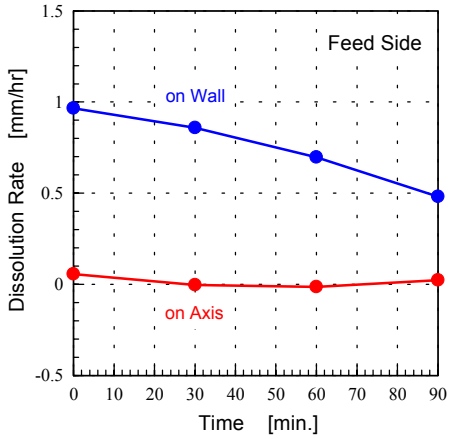

(f) 1 *g*

Fig. 13 Time Evolutions of Dissolution Rate at Feed Side

Conclusions

The numerical code has been developed in order to understand the TLZ method. From the calculation results, it is found that the TLZ method has several features; (i) the growth occurs spontaneously at the seed side and the melting occurs spontaneously at the feed side, (ii) the thermal and the mass transports can easily become diffusion-dominant. Especially the first feature is valuable because it is easy to obtain a homogeneous crystal by synchronizing the furnace translation rate with the spontaneous growth rate.

The limitations of the TLZ method are also investigated. The weakness of the TLZ method is that there is the maximal growth length, which should depend on the initial zone width. The maximal growth length might be longer by spreading the zone width, but the wider zone makes the sustenance of the TLZ mode more difficult. But it is long enough to analyze crystal characteristics and to make a test device under the current boundary conditions.

Acknowledgement

The authors are thankful to Prof. Maekawa at Toyo Univ. for his valuable advice and discussion. We are also grateful to Dr. Matsumoto at National Space Development Agency of Japan for his appropriate suggestions.

References

[1] K. Kinoshita, H. Kato, M. Iwai, T. Tsuru, Y. Muramatsu, S. Yoda: J. Cryst. Growth **225** (2001) 59-66.

[2] K. Nakajima, T. Kusunoki and C. Takenaka: J. Cryst. Growth **113** (1991) 485-490.

[3] J. F. Thompson, F. C. Thames and C. W. Mastin: J. Comp. Phys. **15** (1974) 299.

[4] K. Fujii: *Numerical Methods for Computational Fluid Dynamics* (Tokyo Univ., Tokyo, 1994) 2nd ed., Chap. 7 [in Japanese].

[5] H. Takami and T. Kawamura: *Numerical Solution of Partial Differential Equations by the Finite Difference Method* (Tokyo Univ., Tokyo, 1994) 2nd ed., Chap. 6 [in Japanese].

[6] M. Saitou: Inst. Electron. Mater. Tech. Note **7** (1989) No. 2, 15 [in Japanese].

[7] J. S. Szmyd and K. Suzuki (Ed.): *Modeling of Transport Phenomena in Crystal Growth* (WIT Press, Southampton, 2000), Chap. 4.

[8] S. Adachi, K. Kawachi, M. Kaneko, H. Kato, S. Yoda and K. Kinoshita: *Reliability Investigation on Numerical Analysis by Comparison with Experimental Result* (Annual Report of the Semiconductor Team in NASDA Space Utilization Research Program, 2000).